

Backscattering Study of Electrons from 0.1 to 3.4 MeV

M. Kanafani,¹ X. Fléchard,^{1,*} O. Naviliat-Cuncic,^{1, 2, 3} R. Garreau,¹ T.E. Haugen,^{2, 4} L. Hayen,¹ S. Leblond,⁵ E. Liénard,¹ X. Mougeot,⁵ G. Quéméner,¹ A. Rani,¹ J-C. Thomas,⁶ and S. Vanlangendonck⁷

¹Université de Caen Normandie, ENSICAEN, CNRS/IN2P3, LPC Caen, UMR6534, 14000 Caen, France

²Facility for Rare Isotope Beams and Department of Physics and
Astronomy, Michigan State University, East Lansing 48824 MI, USA

³International Research Laboratory Nuclear Physics and Nuclear Astrophysics, CNRS-MSU, East Lansing 48824 MI, USA

⁴Radiation Physics Division, National Institute of Standards and
Technology, 100 Bureau Drive, Gaithersburg, Maryland 20899, USA

⁵Université Paris-Saclay, CEA, List, Laboratoire National Henri Becquerel (LNE-LNHB), 91120 Palaiseau, France

⁶GANIL, CEA/DRF-CNRS/IN2P3, 14076 Caen, France

⁷KU Leuven, Instituut voor Kern- en Stralingsfysica, 3001 Leuven, Belgium

(Dated: December 1, 2025)

Benchmarking simulation codes for electron transport and scattering in matter is a crucial step for estimating uncertainties in many applications. However, experimental data for electron energies of a few MeV is scarce to make such comparisons. We report here the measurement and the quantitative analysis of backscattering probabilities of electrons in the energy range 0.1 to 3.4 MeV impinging on a YAP:Ce scintillator. The setup consists of a $2 \times 2\pi$ calorimeter which enables, in particular, the inclusion of large incidence angles. The results are used to benchmark various scattering models incorporated in Geant4, showing relative deviations smaller than 5% between experiment and simulations. They demonstrate the current rather high reliability of the simulations when employing appropriate electromagnetic Physics Lists.

I. INTRODUCTION

Tracking particles through matter using Monte Carlo transport codes is an essential tool for designing experiments and for analyzing data in various fields, including high-energy physics, astroparticle physics, nuclear physics, as well as space and medical applications. Among the many physical processes involved in the simulations, electron scattering in matter is a critical component. Benchmarking the performance of scattering models in simulation codes is crucial for estimating uncertainties associated with the results from such codes. For example, precision correlation measurements in nuclear and neutron beta decay [1–7] are often limited by the estimated uncertainties associated with simulations. These must accurately model the scattering of electrons or positrons in the detectors and surrounding materials. Considering the wide range of beta transitions of interest, obtaining benchmarking data for energies in the few MeV range is important.

Several dedicated electron backscattering studies have been carried out in the past [8–12], with various degrees of quantitative analyses. Wright and Trump reported measurements on thick metal targets, at normal incidences and for five energies between 1 and 3 MeV [13], but no quantitative comparison was provided. Such measurements were extended by Tabata from 3.4 to 14 MeV on various targets [8], indicating significant deviations from simple calculations, in particular for the angular distributions. Martin *et al.* performed measurements

at the single energy of 124 keV, in beryllium and silicon [9] and in plastic scintillators [10] at normal incidence. Due to significant systematic uncertainties (up to 23%), the comparison to Geant4 and Penelope simulations used free scaling factors, which makes it difficult to provide a precise quantitative assessment of the overall agreement. Relative comparisons with Geant4 simulations have also been reported in Ref. [11] from measurements using ^{60}Co and ^{207}Bi sources on silicon detectors. Because of the complexity of the source spectra, the conclusions are not straightforward and no quantitative benchmark on backscattering is provided. A dedicated spectrometer has been designed for this purpose [14] but no systematic quantitative study of backscattering has been published so far with such a tool. More recently, Spreng *et al.* performed measurements using an electron gun, finding consistent results with Geant4 simulations within the quoted uncertainties [12]. However, this study covered electron energies up to 10 keV. A comprehensive open-access database, compiling electron backscattering coefficient measurements published before 2023 is available in Ref. [15].

Several systematic evaluations of the Geant4 performance, using different electromagnetic physics models and for electron energies extending up to 15 MeV, have been published in the last decade [16–18]. These stressed in particular how critical some geometry and tracking parameters could be, for several versions of Geant4. The review by Dondero *et al.* showed that measurements conducted in the 1960s and the 1970s, display variations of up to 22% in the backscattering probabilities, for energies smaller than 100 keV at normal incidence on aluminum targets [18]. Some of these measurements are fairly well reproduced by Geant4 simulations. The most stringent

* Corresponding author: flechard@lpccaen.in2p3.fr

tests, in the energy range from 100 keV to 1 MeV [18], used measurements carried out at the Sandia National Laboratories [19, 20] on several targets (C, Al, Mo, Ta and U) at normal incidence, as well as for incident angles up to 75° for Al targets. Comparison with the Geant4 single scattering model at normal incidence shows generally good agreement [18], with relative deviations mostly below 5% for the low-mass targets (C and Al). However, discrepancies up to 15% were observed for higher mass targets or different incidence angles, in particular for energies below 200 keV.

In the present work, we have studied the backscattering of electrons in the energy range 0.1 to 3.4 MeV, including incidence angles from 0 to 90°. The measurements have been carried out using beta particles from ${}^6\text{He}$ decay and YAlO_3 Ce-doped inorganic scintillators (YAP) [21, 22] which serve as active scattering media. The results have been compared with predictions from different electromagnetic Physics Lists of Geant4, to benchmark this code in the considered energy range. The experimental data that support the findings of this article are openly available [23].

II. EXPERIMENTAL SETUP

The experimental setup is described in detail in Ref. [24]. Only key features are summarized below.

A 25 keV ${}^6\text{He}^+$ ion beam, with a typical intensity of 10^4 pps, was produced and delivered by the LIRAT-SPIRAL1 beam line at the GANIL facility in Caen, France. The beam was chopped with a fast electrostatic deflector, enabling the implementation of cycles with implantation and decay phases.

Before entering the detection chamber (Fig. 1), the beam was collimated using two sets of \varnothing 6 mm rings. It was further collimated by a \varnothing 4 mm aperture and implanted on the surface of a YAP crystal scintillator during a time interval of 2.5 s.

The implantation detector (Det. 1 in Fig. 1) was fixed in the chamber. After implantation, a movable detector (Det. 2), mounted on a fast actuator, was brought into contact with the fixed detector [Fig. 1 (b)], creating a 4π geometry around the location of implantation. Moving Det. 2 from the implantation to the detection configurations took about 0.8 s, and returning to the implantation configuration took 1.7 s. The total duration of the cycle was 17 s. In the analysis, a decay time window of 12 s was selected during the beam-off phase.

Each detector consists of a cylindrical ($\varnothing 30$ mm \times 30 mm) YAP:Ce scintillator, surrounded by a plastic (PVT) scintillator (EJ-204), which serves as a veto (Fig. 2). Both scintillators are arranged in a phoswich configuration and are readout by a single Hamamatsu R7723 photomultiplier tube (PMT). The signals from the PMTs, along with a fast signal synchronized with the chopper, were sent to three channels of the FASTER digital data acquisition system [25] configured in a

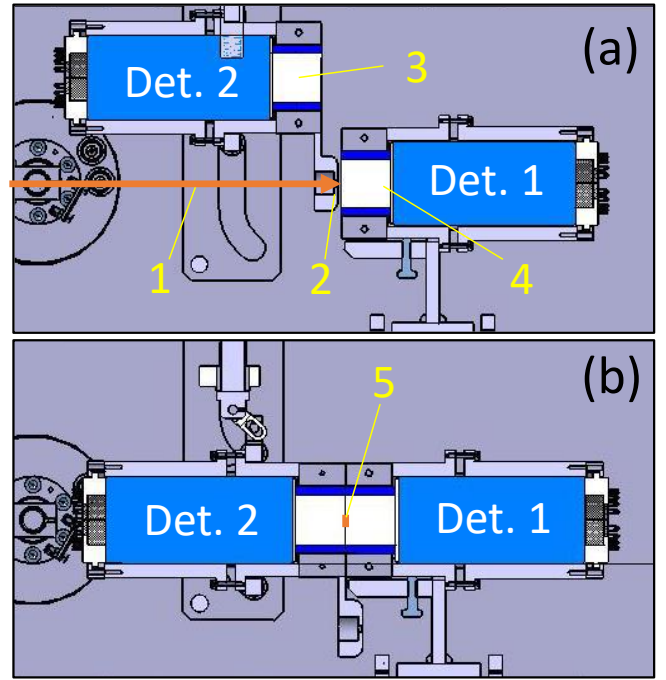


FIG. 1. Sectional views of the detection setup for respectively (a) the implantation and, (b) the detection configurations. The labels indicate the ${}^6\text{He}^+$ beam (1), the \varnothing 4 mm collimator (2), the two YAP scintillators (3,4) and the beam implantation region (5).

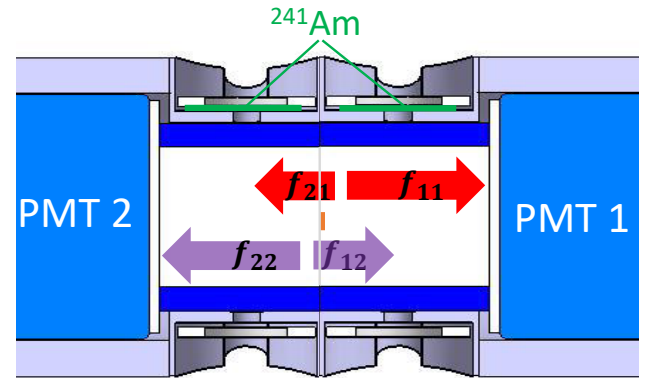


FIG. 2. Sectional view of the detector assembly in the measuring configuration. The red and purple arrows indicate the scintillation light distributed between the two detectors. The f_{ij} coefficient inside an arrow corresponds to the fraction of light collected by PMT i and originating from YAP crystal j .

TDC/QDC mode. A pulse shape analysis technique [24] was implemented to discriminate signals originating from the YAP or from the PVT, based on their different time responses (27 ns decay time for YAP and 2.5 ns for PVT). Two 5 kBq ${}^{241}\text{Am}$ calibration sources, fixed on the side of each detector, were used to perform crude energy calibrations and to correct for gain variations. No light reflector was used on the contact surface of the scintillators, ensuring that no dead layer affects the electron energy

measurements.

According to TRIM calculations [26], the 25 keV ${}^6\text{He}^+$ beam was implanted at a depth of 130 nm inside Det. 1. The diffusion of ${}^6\text{He}$ atoms was estimated to be negligible [24]. The decay of ${}^6\text{He}$ nuclei provided a source of electrons with kinetic energies up to 3.5 MeV. The two YAP scintillators, which enclose the ${}^6\text{He}$ source, serve both as scattering targets and as calorimeters. The backscattering probability is deduced from events recorded in coincidence between the two YAP, for which the electrons deposited some energy in each detector. Since beta particles are emitted isotropically over a 4π sr solid angle, the backscattering probabilities measured as a function of the total recorded energy encompass also large incidence angles (up to 90°), which have not been accessed experimentally so far at these energies.

III. EXPERIMENTAL DATA

Due to the optical coupling between the two scintillators, a fraction ($\approx 20\%$) of the light emitted by one scintillator crosses the interface and is collected by the PMT of the opposite detector. This is schematically shown by the red and purple arrows in Fig. 2. Coincidence events show that both detection channels are triggered provided the total energy deposited is larger than 50 keV.

The construction of the main 2D histogram, used in the data analysis, involves three main steps: the background subtraction, the detector calibration and the crosstalk correction. However, as shown in Appendix B, the last two steps are coupled and must be addressed simultaneously. The background sources and the procedure for background subtraction are detailed in Appendix A.

For each event, the primary signals are the charges collected from the PMTs along with the time stamp within the implantation-decay cycle. A first crude calibration of the two YAP detectors was obtained using the 59.54 keV peaks from the ${}^{241}\text{Am}$ sources, without involving any offset. As previously described in Ref. [24], this first calibration step includes a percent level rate-dependent correction of the PMT gains. This crude calibration is approximate at the few percent level when applied to decay electrons, mainly due to the difference in light collection efficiency for scintillation photons emitted near the ${}^{241}\text{Am}$ source compared to those emitted close to the front surface of the detector, where ${}^6\text{He}$ is implanted. Moreover, this calibration does not account for light crosstalk and cannot be applied to events where the total energy is shared between the two detectors. The resulting 2D energy histogram of the two collected energies is shown in Fig. 3 for events registered during the first half of the decay window (0 to 6 s), which is dominated by ${}^6\text{He}$ decay events, after subtraction of events in the second half of the window (6 to 12 s) which is dominated by background.

The two most intense distributions which look like lines in Fig. 3, correspond to electrons which deposited their

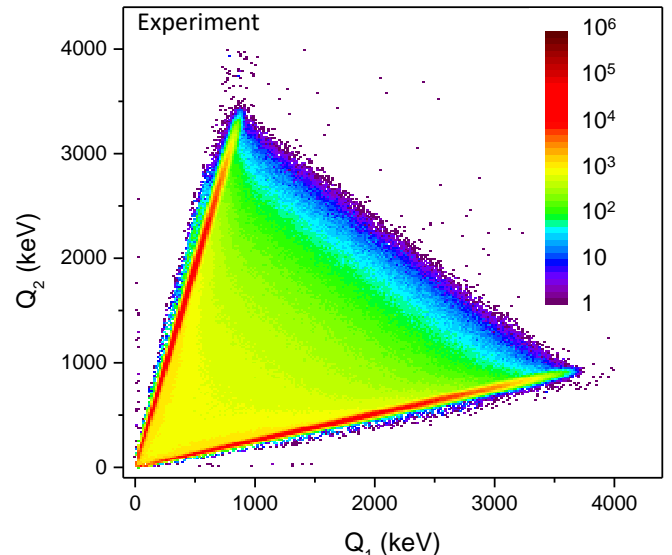


FIG. 3. 2D histogram registered during the first half of the decay window showing the energy collected in Det. 2 (Q_2) versus the energy collected in Det. 1 (Q_1), after background subtraction and a crude energy calibration.

full energy either in Det. 1 or in Det. 2. The slopes of these lines result from the light crosstalk, in which part of the light emitted by one detector is collected by the PMT of the other detector (Fig. 2). Events registered between these two lines are then attributed to electrons that scattered from one detector to the other. For these events, determining the energy deposited in each scintillator requires the light transmission efficiencies to be known. These are denoted by coefficients f_{ij} (Fig. 2), where i indicates the PMT that collected the light and j the YAP scintillator where the light was produced. A refined calibration procedure has been applied to account for this crosstalk, and is detailed in Appendix B. The resulting 2D histogram after background subtraction and calibration, including the crosstalk correction, is shown in Fig. 4.

The histogram in Fig. 4 provides information on both, the nature of the event (backscattered or not) and the total energy deposited, $E_{\text{sum}} = E_1 + E_2$. For a given total energy, the fraction of events between the two main distributions provides then an estimate of the backscattering probability.

IV. GEANT4 SIMULATIONS

A. Geometry and event generator

Geant4 (v11.1.2) was used to generate 10^9 events of beta particles following the decay spectrum of ${}^6\text{He}$, and to record the energies, E_1 and E_2 , deposited in the YAP detectors. The particles were emitted isotropically, over a 4π sr solid angle, from a source located 130 nm inside

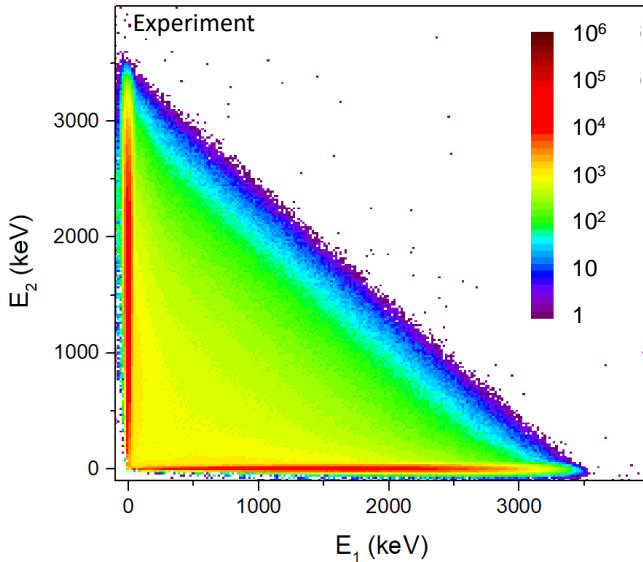


FIG. 4. 2D histogram collected during the first half of the decay window, after background subtraction, calibration and optical crosstalk correction.

Det. 1. The shape of the electron source was assumed to be a uniform disc, with \varnothing 4mm (determined by the last collimator), along the radial direction, and a Gaussian distribution, with 47 nm standard deviation along the beam direction (from TRIM calculations [26]). The energy spectrum of beta particles from ${}^6\text{He}$ decay incorporated all corrections to the phase space, including radiative and hadronic ones [27]. The implemented setup geometry is shown in Fig. 2, and includes the two YAP crystals, the PVT scintillators, the PMTs, and the aluminum detector housing.

B. Physics Lists

The following Physics Lists, included in the Geant4 package, have been considered in the simulations, along with the abbreviations used in the text below:

- G4EmStandardPhysics (Option0)
- G4EmStandardPhysics_option3 (Option3)
- G4EmStandardPhysics_option4 (Option4)
- G4EmLivermorePhysics (Livermore)
- G4EmPenelopePhysics (Penelope)
- G4EmStandardSS (SS)

Option0 is the default electromagnetic (EM) configuration optimized for high-energy physics and is expected to be applicable in processes down to 100 keV. It is based on the Urban Multiple Scattering Model (UrbanMsc) [28] for electrons and positrons. Livermore and Penelope are

specific configurations optimized for low-energy processes and Option4 is a combination of the most accurate EM models. All of these use the Goudsmit-Saunderson multiple scattering model for electrons and are recommended for low-energy precision studies. Note that a new and more performant version of this model was fully implemented in version v10.6 of Geant4 [29]. Option3 is also based on the UrbanMsc model, but is expected to be more accurate than Option0 for the low-energy regime. It is faster than Option4 and may be considered as an intermediate alternative between Option0 and Option4. SS, based on a single scattering model, is by far more demanding in process time, but is expected to yield the most accurate results for electron scattering. For Option4, Penelope, and Livermore, a combination of multiple scattering and single scattering is implemented for large-angle scattering. Livermore and Option4 use the same models for electrons, and so provided equivalent results in all aspects. Only the results from Option4 will thus be shown in the following.

Default values were adopted for the relevant tracking parameters and for the secondary particle creation energy thresholds. For all but SS, 10^9 events were generated whereas for SS, 10^8 events were used because of the much longer computing time. For illustration, the CPU time required for the simulation of 10^6 events is reported in Table I for each Physics List. Those obtained with Option4, Livermore, and Penelope, which are optimized for low-energy processes, are larger by less than a factor of two compared to Option0 and Option3. With SS, the process time is larger by more than two orders of magnitude.

TABLE I. Process (CPU) times using Intel® Xeon® Gold 6246R CPU @ 3.4 GHz processors for the simulation of 10^6 ${}^6\text{He}$ decay events, under the conditions described in Sec. IV A for the six considered Physics Lists.

EM Physics List	CPU time (s)
Option0	1594
Option3	1636
Option4	2692
Livermore	2608
Penelope	2722
SS	640653

C. Calculated Backscattering Probabilities

Consider a source with electrons emitted over an hemisphere, with solid angle $\Omega_1 = 2\pi$ sr. A common definition of the backscattering probability, which is adopted here in a first calculation, is given by the ratio between the number of particles detected in the other hemisphere relative to the total number of particles emitted over Ω_1 . To determine the backscattering probabilities from the simulations, electrons generated over the 2π hemisphere

covered by Det. 1, were selected among all the isotropically generated events. This detector is then considered as the “target” medium. We define θ as the angle between the ${}^6\text{He}$ beam direction and the initial direction of the emitted beta particle. This coincides with the emission angle relative to the cylindrical axis of the YAP detector.

In the simulations, an event was tagged as backscattered when some energy was deposited in Det. 2. Such a definition includes naturally events for which, at any step during slowing down, the electron deposits some of its energy into Det. 2, even when it finally stops in Det. 1. It also includes events for which the electron does not actually escape from Det. 1 but, energy from secondary particles (bremsstrahlung photons, X-rays, etc.) is deposited in Det. 2. Following the definition above, the backscattering probability is then calculated from the ratio between the number of events for which some energy was deposited in Det. 2 relative to the number of generated events over the 2π sr hemisphere. This number can be considered within some energy or angular window. For later use, we denote by $R_{\text{sim}1}$ these probabilities.

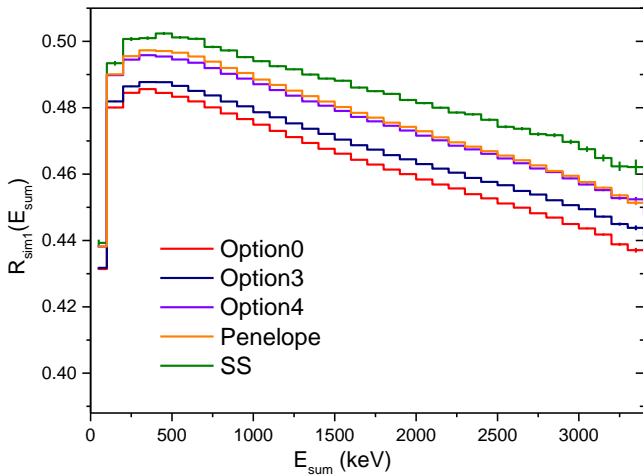


FIG. 5. Backscattering probability $R_{\text{sim}1}$ obtained from Geant4 simulations as a function of the total deposited energy, for five Physics Lists. The energy bin width is 100 keV. The error bars are only statistical, at 1σ , and are visible at the extremes of the spectrum.

The probabilities $R_{\text{sim}1}$ as a function of energy, obtained as described above for the different Physics Lists, are shown in Fig. 5 as a function of the total deposited energy. We observe that they range from 0.43 to 0.51, with a maximum reached for an initial energy close to 500 keV. It is notable that more refined and more computationally demanding models predict larger backscattering probabilities. The relative difference between the two extreme models (SS and Option0) is of the order of 4% to 5% between 500 keV and 3500 keV, and approximately 2% for energies below 100 keV.

The backscattering probabilities as a function of the initial angle θ , weighted for the solid angle, are shown in

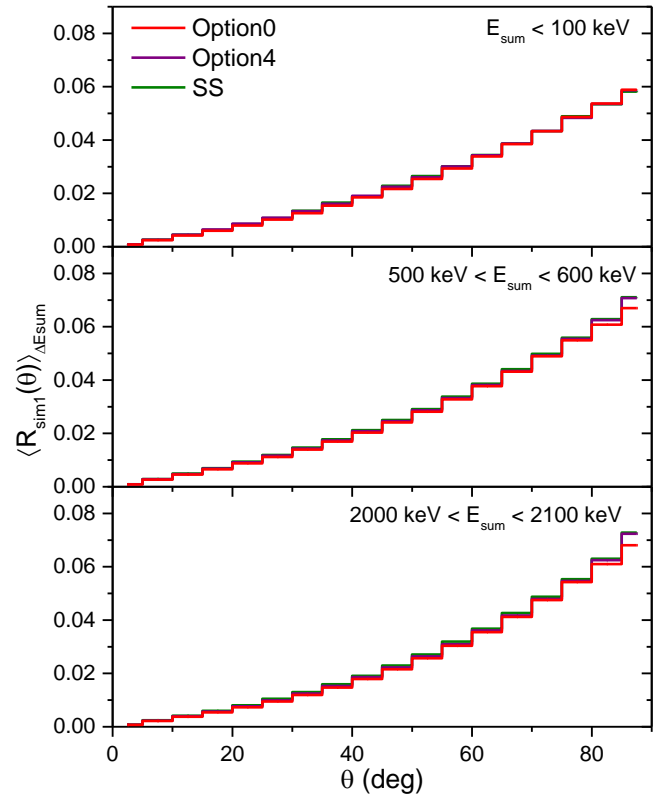


FIG. 6. Backscattering probabilities $R_{\text{sim}1}$, weighted by the solid angle as a function of incident angle θ for an isotropic emission over 2π sr and for three energy intervals ΔE_{sum} . The bin width is 5° .

Fig. 6 for three intervals of the total deposited energy. Only results from Option0, Option4 and SS are shown since the results from Penelope were found to be similar to those from Option4, whereas Option3 provided intermediate results between those of Option0 and Option4.

As expected, the backscattering probability increases with incident angles. Due to the larger solid angle with increasing θ , the relative contribution of large incidence angles is enhanced. At low energies (Fig. 6, top panel), the models do not display any difference at this level of precision. Above 500 keV (Fig. 6, middle and bottom panels), the dominant deviation between Option0 and the other models is observed at angles larger than 80° . This highlights the significant impact of large incidence angles, in particular, above 80° , whose contributions are included in the present study.

V. ANALYSIS METHOD

The selection of events with $\theta \leq \pi/2$, made in the simulation, cannot be applied to the experimental data for which the only available information is the energy deposited in each detector. In this section, we present the method used for the analysis of the experimental spec-

trum shown in Fig. 4 to extract the backscattering probabilities. The description of the method is done using a simulated 2D histogram, obtained with Option4 and shown in Fig. 7, which includes the convolution with the detector response, as described in Appendix B.

A. General Principle

Consider events with an energy deposited in Det. 1 which is larger than the energy deposited in Det. 2. These events are located below the main diagonal line in the 2D histogram of Fig. 7. The dominant horizontal distribution, which appears as a line, is again due to electrons depositing their full energy in Det. 1, without backscattering. These events will be termed “single-detector events” (SDE). Due to the very shallow implantation depth (130 nm) in the volume of Det. 1, these events can, to first order, be assimilated to electrons initially emitted towards Det. 1. Since simulations give access to the exact deposited energy (before convolution with the detector resolution), SDE are unambiguously identified in the simulated data by imposing no energy deposition in Det. 2. The other events, distributed over the triangle below the main diagonal and the SDE, are labeled “two-detector events” (TDE) and arise from electrons backscattering in one of the two detectors. Simulations indicate that a significant fraction ($\approx 24\%$) of electrons emitted towards Det. 1 that are backscattered in Det. 2 actually deposit more energy in Det. 2 than in Det. 1. However, because of the almost fully symmetric detection setup, those events are mirrored by electrons emitted towards Det. 2 and backscattering with a larger energy deposited in Det. 1, and are then part of TDE. In the following, we thus assimilate TDE with backscattered events for which $E_1 \geq E_2$ and SDE with non-backscattered events.

Next, we select a narrow energy interval around a given total energy, $E_{\text{sum}} = E_1 + E_2$ (grey band in Fig. 7). Since the simulation provides the identification of the event, it enables to build separately the distributions for SDE and TDE (upper panel in Fig. 7). If $N_{\text{sim}}^{\text{SD}}$ and $N_{\text{sim}}^{\text{TD}}$ denote respectively the number of SDE and TDE obtained from the simulations, then the ratio

$$R_{\text{sim}2} = \frac{N_{\text{sim}}^{\text{TD}}}{N_{\text{sim}}^{\text{SD}} + N_{\text{sim}}^{\text{TD}}} , \quad (1)$$

provides an estimate of the backscattering probability. We note that this ratio is independent of the convolution since the simulation gives unambiguously access to the type of event, SDE or TDE, before applying the convolution with the detector response function. In other words, $N_{\text{sim}}^{\text{TD}}$ and $N_{\text{sim}}^{\text{SD}}$ are the integrals of the distributions shown in the upper panel of Fig. 7.

The procedure above is then repeated for each Physics List to build the simulated 2D histogram from which the SDE and TDE distributions are determined.

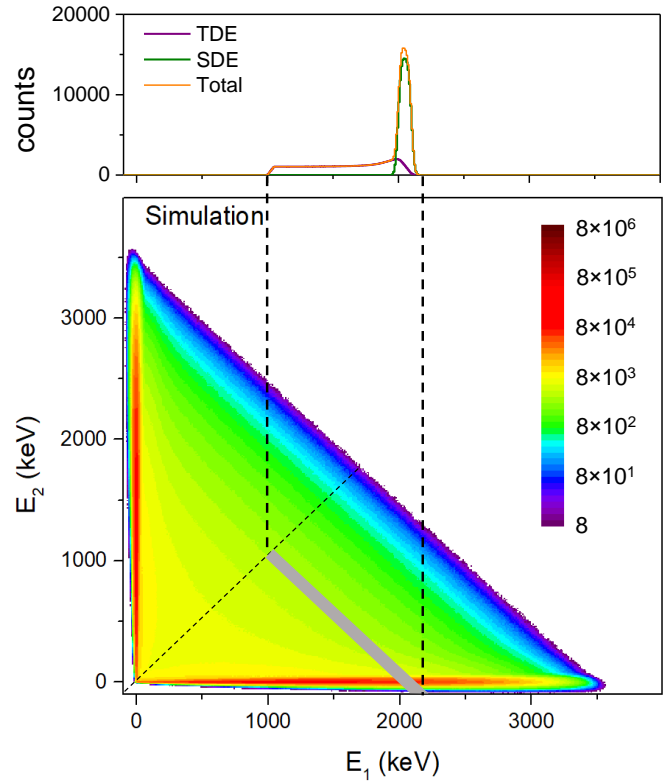


FIG. 7. 2D histogram obtained from simulations with Option4, after convolution with the detector response. The gray band indicates the selection of events with total deposited energy between 2000 keV and 2100 keV with $E_1 \geq E_2$. The upper panel shows the distributions SDE (green), TDE (purple) and total (orange) as a function of E_1 .

It is worth noting that the 130 nm implantation depth of the ${}^6\text{He}$ ions inside Det. 1, implemented in the simulation, breaks the symmetry of the detection system. The ratio $R_{\text{sim}2}$, which is directly comparable to experimental data, is therefore not strictly equivalent to the ratio $R_{\text{sim}1}$ which quantifies the real backscattering probability of electrons hitting the surface of a YAP crystal. This difference is discussed in Sec. V B.

A similar analysis for events with $E_2 \geq E_1$ would have been valuable as well. However, a clean definition of a SDE for Det. 2 is impossible for such a condition. Due to the implantation in Det. 1, all electrons do deposit some energy in Det. 1 prior to reaching Det. 2. Such analysis would have required the use of an arbitrary energy threshold whose effect is difficult to interpret.

B. Comparison Test

The ratio $R_{\text{sim}2}$ is shown in Fig. 8 (a) as a function of the total deposited energy obtained with the five Physics Lists. This plot shows very similar features to those of Fig. 5, where the $R_{\text{sim}1}$ backscattering probabilities were determined by selecting electrons emitted only towards

Det. 1 and requesting energy deposition in Det. 2. The ratio $R_{\text{sim}2}$ is systematically lower than $R_{\text{sim}1}$, as shown in Fig. 8 (b). For the lowest-energy bin, centered at 50 keV, the absolute difference is ≈ 0.04 . The difference quickly decreases to ≈ 0.008 at 500 keV and further down to ≈ 0.002 at 3000 keV, for all Physics Lists.

All Physics Lists produce the same differences ($R_{\text{sim}1} - R_{\text{sim}2}$) as a function of the total energy [Fig. 8 (b)]. This suggests that these discrepancies are related to the difference in the definition of backscattering probabilities associated with $R_{\text{sim}1}$ (Sec. IV C) and $R_{\text{sim}2}$ in Eq. (1). It also shows that both definitions are equally valid for testing and comparing the different Physics Lists. This difference is due to the small but still significant implantation depth of ${}^6\text{He}$ in Det. 1. A small fraction of the electrons emitted towards Det. 2 can backscatter before reaching Det. 2 and leads to a larger value of $N_{\text{sim}}^{\text{SD}}$ and hence to a reduction of $R_{\text{sim}2}$.

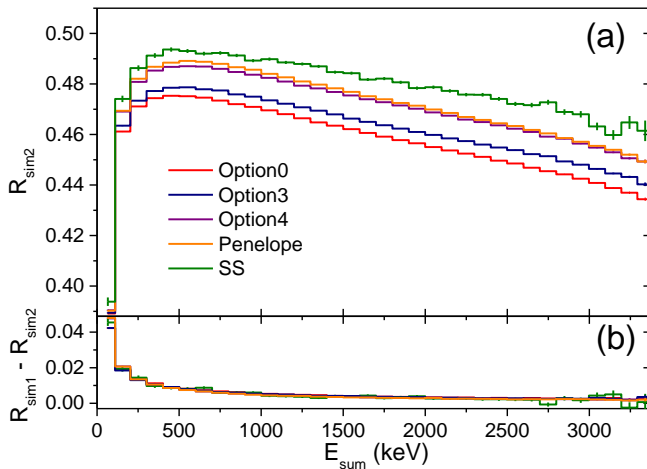


FIG. 8. (a): Ratio $R_{\text{sim}2}$ as a function of the total deposited energy for the different Physics Lists; (b): Difference ($R_{\text{sim}1} - R_{\text{sim}2}$) between the backscattering probabilities deduced from Fig. 5 and from panel (a) above. The energy bin width is 100 keV. Error bars are only statistical, at 1σ .

C. Application to Experimental Data

The same energy cuts as those applied to the simulation histograms, are then applied to the experimental 2D histogram in Fig. 4. The projection of events along the E_1 axis gives a single distribution which contains an unknown mixture of SDE and TDE events. To unravel the two contributions, this single distribution is then fitted with a linear combination of the SDE and TDE distributions deduced from the simulation, with the same energy cuts and accounting for the detector resolution as determined in Appendix B. From the fitted distributions, one deduces then the integrals $N_{\text{exp}}^{\text{SD}}$ and $N_{\text{exp}}^{\text{TD}}$ which are used

to calculate the corresponding experimental ratio

$$R_{\text{exp}} = \frac{N_{\text{exp}}^{\text{TD}}}{N_{\text{exp}}^{\text{SD}} + N_{\text{exp}}^{\text{TD}}} . \quad (2)$$

VI. RESULTS

The energy distributions projected along E_1 , for the simulation and the experimental data, have been analyzed for 33 windows of the total deposited energy. The lower edge of the windows ranged from 100 to 3300 keV and the window width was 100 keV. Data with a total energy smaller than 100 keV or larger than 3400 keV were discarded due to poor statistics. The distributions obtained using Option4 are compared to the experimental ones in Fig. 9 for five energy windows. The lines in green and purple correspond, respectively, to SDE and TDE from the simulation. The histograms in black show the experimental data, after normalization to the total number of simulated events. The orange lines represent the fits of the experimental spectra using a linear combination of SDE and TDE distributions from simulations.

We denote by s_1 and s_2 the scaling factors for, respectively, SDE and TDE distributions. These are the only free parameters of the fits to precisely adjust both the backscattering probability and the number of events in each energy selection. The experimental ratio in Eq. (2) has then been estimated using the fitted parameters, with

$$N_{\text{exp}}^{\text{SD}} = s_1 N_{\text{sim}}^{\text{SD}} , \quad (3)$$

$$N_{\text{exp}}^{\text{TD}} = s_2 N_{\text{sim}}^{\text{TD}} . \quad (4)$$

In Fig. 9, the backscattering tail (purple line) from TDE nicely follows the experimental data for all five energy windows. The result of the fit (in orange) also matches the experimental data for all windows and over the full spectra. This demonstrates not only that the simulation using Option4 reproduces remarkably well the relative amount of backscattered events but also the energy distribution between the two detectors.

The tails corresponding to TDE obtained with four different Physics Lists are compared to the experimental data in Fig. 10 for four windows of the total deposited energy. The distributions obtained with Penelope were equivalent to those obtained with Option4 and are not shown. For all energy windows, the results obtained with Option4 and SS reproduce the experimental data fairly well. This is not so for Option0 and Option3, which overestimate the backscattering tail in the region of the spectrum at 100 keV to 200 keV below the main SDE peak. The discrepancies also increase at higher total energies. At the same time, simulations with Option0 and Option3 underestimate backscattering events, depositing less than 50 keV in Det. 2, located in the region underneath the SDE peak.

Finally, the experimental backscattering probability, R_{exp} , was extracted using the distributions obtained

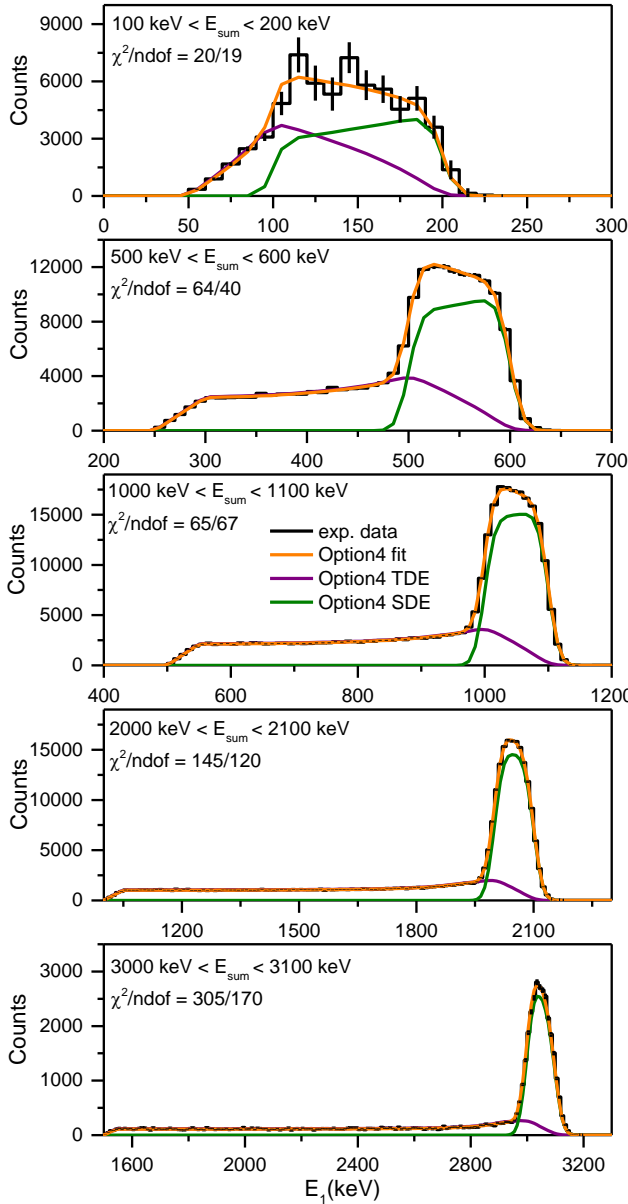


FIG. 9. Fit of the experimental data (black histograms) with energy distributions obtained with Option4 for five intervals of the total deposited energy. The green and purple lines correspond respectively to the SDE and TDE distributions. Orange curves are fits to the data. The statistical uncertainties are at 1σ .

from each simulation and the fitting procedure described above. The ratio $R_{\text{sim}2}$ was then compared to the corresponding R_{exp} ratio extracted, in a self-consistent way, using the distributions from that same simulation. Note that the shape differences for the TDE distributions shown in Fig. 10 also affect the ratio R_{exp} extracted using the different models.

Figure 11 shows the difference, $(R_{\text{sim}2} - R_{\text{exp}})$ between the ratios from simulations and from experimental data for each Physics List. The error bars indicate the statis-

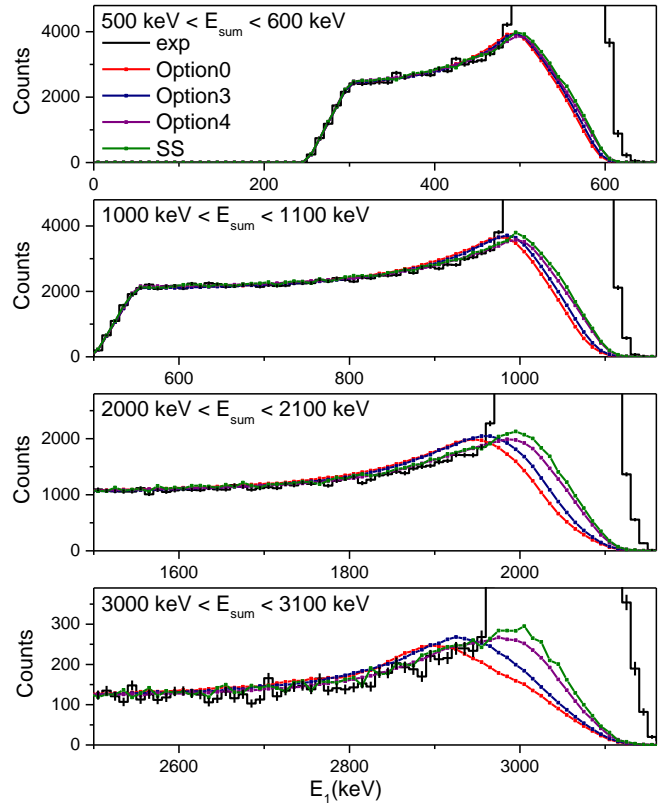


FIG. 10. Comparison of the TDE distributions obtained from simulations, using the different Physics Lists, with experimental data normalized to the total number of simulated events. The uncertainties on the experimental spectra are at 1σ .

tical uncertainty, dominated by the experimental data. The light gray area indicates the systematic uncertainty due to a possible calibration mismatch of at most 2.5 keV.

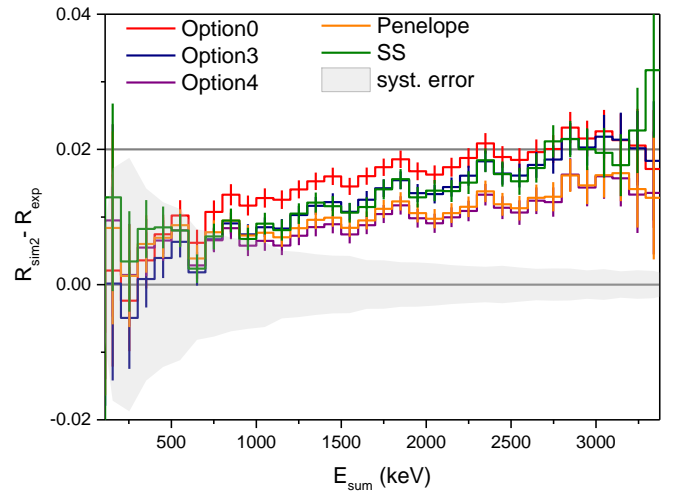


FIG. 11. Difference between the ratios $R_{\text{sim}2}$ and R_{exp} obtained using the different Physics Lists. The statistical uncertainties are at 1σ . See text for details.

For a total deposited energy below 750 keV, all simulations are consistent with the experimental data, although the statistical uncertainties are of the order of 1%. Above 750 keV, the ratio R_{sim2} is systematically higher than R_{exp} for all Physics Lists. This indicates an overestimate of the backscattering probability by the simulations. Nevertheless, the deviation from the experimental value does not exceed 2% for the largest (Option0), which corresponds to a relative overestimate by less than 5%. For Option4 and Penelope, the deviations are even smaller, with a relative overestimate of the backscattering probability remaining below 3.5%. We remind here that the Livermore Physics List provided results equivalent to those of Option4. Quite surprisingly, the simulation using SS, which was anticipated to be the most accurate, does not outperform Option 4 and Penelope in terms of agreement with experimental data.

VII. CONCLUSIONS

We have determined the backscattering probabilities of electrons impinging on a YAP scintillator with energies from 0.1 to 3.4 MeV. The measurement used a $2 \times 2\pi$ calorimeter, which was originally designed to eliminate the effect of electron backscattering in measurements of beta-energy spectra. The separation of the calorimeter into two halves enabled the precise identification of backscattered events.

The quantitative analysis involves comparisons with simulations to benchmark six Physics Lists incorporated in Geant4. For Option4, Livermore and Penelope, simulations are closer to experimental data in the explored energy range, with relative deviations on the backscattering probabilities reaching 3.5% for the largest incident energies. Moreover, the distributions of the energy loss for backscattered events were properly reproduced with these three Physics Lists as well as with SS. For Option0 and Option3, which are not optimized for low energy processes, the agreement remains quite acceptable, with relative differences in backscattering probabilities below 5%. However, the shape of the experimental backscattering tail is not properly reproduced by these last two Physics Lists. The backscattering probabilities obtained with SS were surprisingly in poorer agreement with experimental data than those with Option4, Livermore and Penelope.

The uncertainties on electron backscattering often represent a significant part of the systematic uncertainty budget for precision measurements in beta decay. Due to the lack of precise benchmarks of Geant4 for the backscattering of electrons in the energy range from 100 keV up to several MeV, conservative relative uncertainties of the order of 10% to 20% have usually been considered. This is particularly the situation for experiments using strong magnetic fields, in which the detection of beta particles produces large incident angles [3].

The agreement obtained in the present work between

simulations and experimental data, which covers a large energy range and includes large incident angles, is rather remarkable. This invites a revision of the conservative approach for estimating the impact of simulations, especially when using the most accurate options such as Option4, Penelope or Livermore. Although the results presented here cannot readily be transposed to other materials or to any arbitrary geometry, it should help mitigating the usually large relative uncertainties considered for backscattering probabilities.

VIII. ACKNOWLEDGEMENTS

The authors thank the technical support from LPC Caen and GANIL staff and are grateful to A. Singh for her assistance during the running of the experiment. This project was supported in part by the Agence Nationale de la Recherche under grant ANR-20-CE31-0007-01 (bSTILED).

IX. DISCLAIMER

Certain trade names and company products are mentioned in the text or identified in illustrations in order to adequately specify the experimental procedure and equipment used. In no case does such identification imply recommendation or endorsement by the National Institute of Standards and Technology nor does it imply that the products are necessarily the best available for the purpose.

Appendix A: Background subtraction

Previous analyses of the ${}^6\text{He}$ decay time spectra performed with the present setup [24], enabled the identification of two main background contributions. The first was due to the constant ambient background, which includes the contribution of the 59.54 keV γ rays from ${}^{241}\text{Am}$. This background was suppressed by subtracting events in the second half (6 to 12 s) of the decay window [Fig. 12 (b)], from those in the first half (0 to 6 s) of the decay window [Fig. 12 (a)]. The second background contribution arises from bremsstrahlung radiation produced by decays of ${}^6\text{He}$ nuclei implanted in the last collimator (Fig.1). This contribution was subtracted using a dedicated background run, in which a 0.4 mm thick Al plate was placed at the exit of the collimator to prevent direct implantation on Det. 1.

The energy distribution of these bremsstrahlung events in the 2D energy histogram is shown in Fig.12 (c). The normalization factor for this background subtraction was determined by suppressing its dominant contribution, peaked close to 100 keV. It was first determined with a few percents precision using the 2D spectra and was subsequently refined through a fit of the total energy spec-

trum after the refined calibration procedure, as described below.

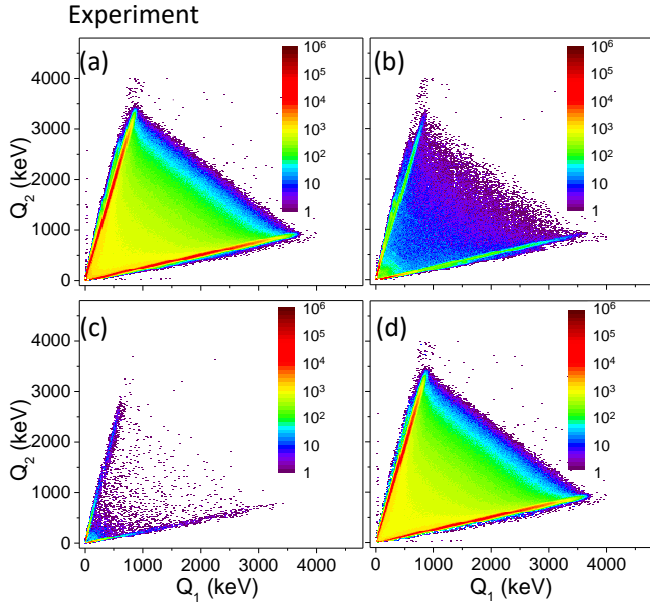


FIG. 12. Experimental 2D histograms for different conditions of the experiment. (a): data from the first half of the decay window (0 to 6 s) dominated by electrons from ${}^6\text{He}$ decay; (b): data from the second half of the decay window (6 to 12 s) dominated by the constant background; (c): data from a dedicated run performed to identify background sources in the absence of implantation; (d): data of the first half of the decay window after background subtraction.

Appendix B: Crosstalk correction and detector resolution

Because of the optical coupling between the two detectors, their calibrations and the determination of their response functions have to be performed simultaneously. After background subtraction, the experimental 2D histogram in Fig. 12 (d) was used, together with Geant4 simulations, to determine the calibration parameters required for an accurate reconstruction of the energies E_1 and E_2 deposited in each detector. These parameters, noted F_{ij} ($i, j = 1, 2$), are proportional to the relative light collection coefficients f_{ij} ($i, j = 1, 2$) illustrated in Fig. 2, and two offsets $Q_{\text{off}1}$ and $Q_{\text{off}2}$. The light transport within the crystals was not included in the simulations since the experimental spectra provide the average transport coefficients. The strong proportionality of YAP crystals compared to other types of scintillators [21, 22] enables the use of a linear relationship between light production and deposited energy such that

$$\begin{pmatrix} Q_1 \\ Q_2 \end{pmatrix} = \begin{pmatrix} F_{11} & F_{12} \\ F_{21} & F_{22} \end{pmatrix} \begin{pmatrix} E_1 \\ E_2 \end{pmatrix} + \begin{pmatrix} Q_{\text{off}1} \\ Q_{\text{off}2} \end{pmatrix} . \quad (\text{B1})$$

TABLE II. Values of the calibration coefficients, offsets, and convolution parameters obtained from the iterative procedure of the refined calibration.

$F_{11} = 1.0652$	$Q_{\text{off}1} = 2.0 \text{ keV}$
$F_{12} = 0.2576$	$Q_{\text{off}2} = 3.5 \text{ keV}$
$F_{22} = 0.9847$	$\alpha_1 = 0.61 \text{ keV}^{1/2}$
$F_{21} = 0.2694$	$\alpha_2 = 0.65 \text{ keV}^{1/2}$

The Option4 simulation (Sec. IV) was used for the refined calibration, with 10^9 events. Estimates of the F_{ij} coefficients were first inferred from the 2D histogram in Fig. 12 (d) using the end point energies and the slopes of the two main distributions, corresponding to a full energy deposition either in Det. 1 or Det. 2. In this first step, the offsets were considered negligible and set to zero. Using these values, Eq. (B1) was then applied to the simulated events, to compute the quantities Q_1 and Q_2 .

The effect of the detector resolution was implemented in the simulation by convolving Q_1 and Q_2 with Gaussian functions having standard deviations $\sigma_1(Q_1)$ and $\sigma_2(Q_2)$. Considering that the dominant contribution to the resolution is the statistical fluctuations associated with the number of photoelectrons collected by the PMTs we have, for each detector,

$$\sigma_i(Q_i) = \alpha_i \sqrt{Q_i} . \quad (\text{B2})$$

In a first crude step, the values of α_i were inferred from the fits of the 59.54 keV gamma peaks [24].

This first procedure produced then a 2D histogram from the simulated data [Fig. 13 (b)] closely matching the experimental one [Fig. 13 (a)]. The refined calibration to improve the precision on the F_{ij} parameters and on possible offsets consisted in an iterative procedure, which makes successive comparisons of the simulated and experimental histograms. We defined 35 successive slices in Q_1 and Q_2 , for the experimental data, having 100 keV width, as illustrated in Fig.13 (a). Their projections are dominated by the SDE (see Sec. V A), which were fitted with Gaussian functions whose mean values, standard deviations and integrals were compared to those obtained with simulated events. The fit range, indicated by dashed red lines in the projections of Fig.13 (a), selects mostly SDE, so that the backscattering tail only has a marginal effect in the calibration. The F_{ij} values and offsets were then updated after several iterations, to minimize the deviation between the fit results from the experimental and simulated spectra. The iteration process was stopped when the deviations on the mean values remained below 2.5 keV over the full 3500 keV range and became dominated by non-linear effects that are not yet implemented in the calibration functions. The α_i parameters were also adjusted during the iteration process, resulting in a change of less than 3% from their initial values. The final precision on the calibration was considered to be more than sufficient for the present study of backscattering probabilities. The calibration parameters obtained are listed in Table II.

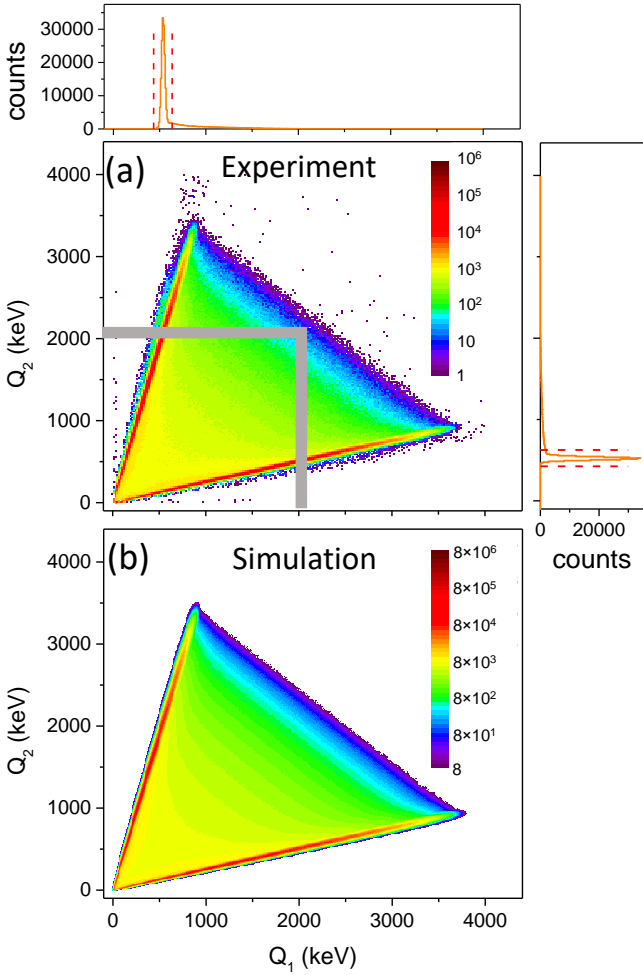


FIG. 13. (a): Illustration of the data selections used for the refined calibration. The dashed red lines on the projected histograms indicate the range for the Gaussian fits of the SDE distributions; (b): 2D energy histogram generated with simulated events using the refined calibration parameters which account for the detector resolution and crosstalk correction.

Appendix C: Total Energy Reconstruction

The procedure described above consisted to match, as close as possible, the simulated 2D histogram to the experimental one. However, the specific shape of the β -particle energy spectrum is not involved in the extraction of the backscattering probabilities. It is included in the simulations in order to match the properties of the electron source.

Using the set of parameters determined above and inverting Eq. (B1), the energies E_1 and E_2 deposited in each detector can be determined,

$$\begin{pmatrix} E_1 \\ E_2 \end{pmatrix} = \frac{1}{d} \begin{pmatrix} F_{22} & -F_{21} \\ -F_{12} & F_{11} \end{pmatrix} \begin{pmatrix} \Delta Q_1 \\ \Delta Q_2 \end{pmatrix}, \quad (C1)$$

where $d = (F_{11}F_{22} - F_{12}F_{21})$ and $\Delta Q_i = (Q_i - Q_{\text{off},i})$. The total deposited energy, $E_{\text{sum}} = E_1 + E_2$, can then

be reconstructed. The resulting 2D histograms obtained for both experimental and simulated data are displayed again in Fig. 14. These are the same 2D histograms as those in Figs. 4 and 7.

The experimental and simulated spectra of the total energy deposited are compared in the upper panel of Fig. 15. The simulated spectrum was adjusted to the experimental one using only two free parameters: the overall scaling factor and the normalization factor for the subtraction of the bremsstrahlung induced background discussed in Appendix A. The lower panel of Fig. 15 shows the standard residuals from the fit. The agreement between the two spectra provides an additional internal consistency check and validates both the background subtraction and the calibration procedure.

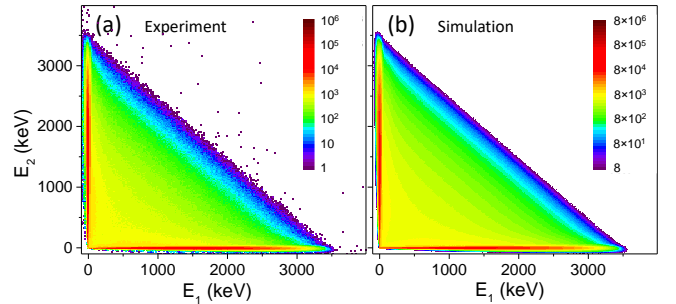


FIG. 14. Experimental (a) and simulated (b) 2D energy histograms of the energy deposited in Det. 1 and Det. 2. The experimental 2D histogram was obtained after background subtraction and includes the refined calibration, whereas the simulated 2D histogram includes the convolution.

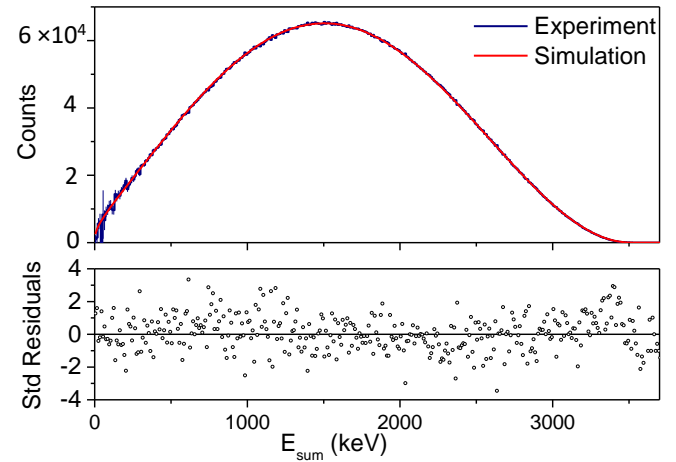


FIG. 15. Upper panel: reconstructed total energy spectrum for the experimental (blue) and simulated (red) data. The larger statistical fluctuations below 300 keV are due to the impact of the large bremsstrahlung background contribution. Lower panel: standard residuals from the fit.

[1] X. Fléchard, Ph. Velten, E. Liénard, A. Méry, D. Rodríguez, G. Ban, D. Durand, F. Mauger, O. Naviliat-Cuncic, and J. C. Thomas. Measurement of the $\beta - \nu$ correlation coefficient $a_{\beta\nu}$ in the β decay of trapped ${}^6\text{He}^+$ ions. *Journal of Physics G: Nuclear and Particle Physics*, 38(5):055101, mar 2011. doi: 10.1088/0954-3899/38/5/055101.

[2] B. Fenker, A. Gorelov, D. Melconian, J. A. Behr, M. Anholm, D. Ashery, R. S. Behling, I. Cohen, I. Craiciu, G. Gwinner, J. McNeil, M. Mehlman, K. Olchanski, P. D. Shidling, S. Smale, and C. L. Warner. Precision measurement of the β asymmetry in spin-polarized ${}^{37}\text{K}$ decay. *Phys. Rev. Lett.*, 120:062502, Feb 2018. URL: <https://link.aps.org/doi/10.1103/PhysRevLett.120.062502>, doi:10.1103/PhysRevLett.120.062502.

[3] V. Araujo-Escalona, D. Atanasov, X. Fléchard, P. Alfaur, P. Ascher, B. Blank, L. Daudin, M. Gerbaux, J. Giovinazzo, S. Grévy, T. Kurtukian-Nieto, E. Liénard, G. Quéméner, N. Severijns, S. Vanlangendonck, M. Versteegen, and D. Zákoucký. Simultaneous measurements of the β -neutrino angular correlation in ${}^{32}\text{Ar}$ pure fermi and pure gamow-teller transitions using β -proton coincidences. *Phys. Rev. C*, 101:055501, May 2020. URL: <https://link.aps.org/doi/10.1103/PhysRevC.101.055501>, doi:10.1103/PhysRevC.101.055501.

[4] H. Saul, C. Roick, H. Abele, H. Mest, M. Klopf, A. K. Petukhov, T. Soldner, X. Wang, D. Werder, and B. Märkisch. Limit on the fierz interference term b from a measurement of the beta asymmetry in neutron decay. *Phys. Rev. Lett.*, 125:112501, Sep 2020. URL: <https://link.aps.org/doi/10.1103/PhysRevLett.125.112501>, doi:10.1103/PhysRevLett.125.112501.

[5] P. Müller, Y. Bagdasarova, R. Hong, A. Leredde, K. G. Bailey, X. Fléchard, A. García, B. Graner, A. Knecht, O. Naviliat-Cuncic, T. P. O'Connor, M. G. Sternberg, D. W. Storm, H. E. Swanson, F. Wauters, and D. W. Zumwalt. β -nuclear-recoil correlation from ${}^6\text{He}$ decay in a laser trap. *Phys. Rev. Lett.*, 129:182502, Oct 2022. URL: <https://link.aps.org/doi/10.1103/PhysRevLett.129.182502>, doi:10.1103/PhysRevLett.129.182502.

[6] M. T. Burkay, G. Savard, A. T. Gallant, N. D. Scielzo, J. A. Clark, T. Y. Hirsh, L. Varriano, G. H. Sargsyan, K. D. Launey, M. Brodeur, D. P. Burdette, E. Heckmaier, K. Joerres, J. W. Klimes, K. Kolos, A. Laminack, K. G. Leach, A. F. Levand, B. Longfellow, B. Maaß, S. T. Marley, G. E. Morgan, P. Mueller, R. Orford, S. W. Padgett, A. Pérez Galván, J. R. Pierce, D. Ray, R. Segel, K. Siegl, K. S. Sharma, and B. S. Wang. Improved limit on tensor currents in the weak interaction from ${}^8\text{Li}$ β decay. *Phys. Rev. Lett.*, 128:202502, May 2022. URL: <https://link.aps.org/doi/10.1103/PhysRevLett.128.202502>, doi:10.1103/PhysRevLett.128.202502.

[7] X. Sun, E. Adamek, B. Allgeier, Y. Bagdasarova, D. B. Berguno, M. Blatnik, T. J. Bowles, L. J. Broussard, M. A.-P. Brown, R. Carr, S. Clayton, C. Cude-Woods, S. Currie, E. B. Dees, X. Ding, B. W. Filippone, A. García, P. Geltenbort, S. Hasan, K. P. Hickerston, J. Hoagland, R. Hong, A. T. Holley, T. M. Ito, A. Knecht, C.-Y. Liu, J. Liu, M. Makela, R. Mammei, J. W. Martin, D. Melconian, M. P. Mendenhall, S. D. Moore, C. L. Morris, S. Nepal, N. Nouri, R. W. Pattie, A. Pérez Gálvan, D. G. Phillips, R. Picker, M. L. Pitt, B. Plaster, D. J. Salvat, A. Saunders, E. I. Sharapov, S. Sjue, S. Slutsky, W. Sondheim, C. Swank, E. Tatar, R. B. Vogelaar, B. VornDick, Z. Wang, W. Wei, J. W. Wexler, T. Womack, C. Wrede, A. R. Young, and B. A. Zeck. Improved limits on fierz interference using asymmetry measurements from the ultracold neutron asymmetry (ucna) experiment. *Phys. Rev. C*, 101:035503, Mar 2020. URL: <https://link.aps.org/doi/10.1103/PhysRevC.101.035503>, doi:10.1103/PhysRevC.101.035503.

[8] Tatsuo Tabata. Backscattering of electrons from 3.2 to 14 mev. *Phys. Rev.*, 162:336–347, Oct 1967. URL: <https://link.aps.org/doi/10.1103/PhysRev.162.336>, doi:10.1103/PhysRev.162.336.

[9] J. W. Martin, J. Yuan, S. A. Hoedl, B. W. Filippone, D. Fong, T. M. Ito, E. Lin, B. Tipton, and A. R. Young. Measurement of electron backscattering in the energy range of neutron β decay. *Phys. Rev. C*, 68:055503, Nov 2003. URL: <https://link.aps.org/doi/10.1103/PhysRevC.68.055503>, doi:10.1103/PhysRevC.68.055503.

[10] J. W. Martin, J. Yuan, M. J. Betancourt, B. W. Filippone, S. A. Hoedl, T. M. Ito, B. Plaster, and A. R. Young. New measurements and quantitative analysis of electron backscattering in the energy range of neutron β -decay. *Phys. Rev. C*, 73:015501, Jan 2006. URL: <https://link.aps.org/doi/10.1103/PhysRevC.73.015501>, doi:10.1103/PhysRevC.73.015501.

[11] G. Soti, F. Wauters, M. Breitenfeldt, P. Finlay, I.S. Kraev, A. Knecht, T. Porobić, D. Zákoucký, and N. Severijns. Performance of geant4 in simulating semiconductor particle detector response in the energy range below 1mev. *Nuclear Instruments and Methods in Physics Research Section A: Accelerators, Spectrometers, Detectors and Associated Equipment*, 728:11–22, 2013. URL: <https://www.sciencedirect.com/science/article/pii/S0168900213008802>, doi:10.1016/j.nima.2013.06.047.

[12] D. Spreng, K. Urban, M. Carminati, F. Edzards, C. Fiorini, P. Lechner, A. Nava, D. Siegmann, C. Wiesinger, and S. Mertens. Investigation of electron backscattering on silicon drift detectors for the sterile neutrino search with tristan. *Journal of Instrumentation*, 19(12):P12009, dec 2024. URL: <https://dx.doi.org/10.1088/1748-0221/19/12/P12009>, doi:10.1088/1748-0221/19/12/P12009.

[13] Kenneth A. Wright and John G. Trump. Back-scattering of megavolt electrons from thick targets. *Journal of Applied Physics*, 33(2):687–690, 02 1962. doi:10.1063/1.1702488.

[14] K. Lojek, D. Rozpedzik, K. Bodek, M. Perkowski, and N. Severijns. Front-end electronics and data acquisition system for a multi-wire 3d gas tracker. *Nuclear Instruments and Methods in Physics Research Section A: Accelerators, Spectrometers, Detectors and Associated Equipment*, 802:38–47, 2015. URL: <https://www.sciencedirect.com/science/article/pii/S0168900215010220>,

doi:10.1016/j.nima.2015.08.058.

[15] Akbari F. A comprehensive open-access database of electron backscattering coefficients for energies ranging from 0.1 kev to 15 mev. *Medical physics*, 50(9):5920–5929, 09 2023. doi:10.1002/mp.16604.

[16] Sung Hun Kim, Maria Grazia Pia, Tullio Basaglia, Min Cheol Han, Gabriela Hoff, Chan Hyeong Kim, and Paolo Saracco. Validation test of geant4 simulation of electron backscattering. *IEEE Transactions on Nuclear Science*, 62(2):451–479, 2015. doi:10.1109/TNS.2015.2401055.

[17] Tullio Basaglia, Min Cheol Han, Gabriela Hoff, Chan Hyeong Kim, Sung Hun Kim, Maria Grazia Pia, and Paolo Saracco. Quantitative test of the evolution of geant4 electron backscattering simulation. *IEEE Transactions on Nuclear Science*, 63(6):2849–2865, 2016. doi:10.1109/TNS.2016.2617834.

[18] Paolo Dondero, Alfonso Mantero, Vladimir Ivanchenko, Simone Lotti, Teresa Mineo, and Valentina Fioretti. Electron backscattering simulation in geant4. *Nuclear Instruments and Methods in Physics Research Section B: Beam Interactions with Materials and Atoms*, 425:18–25, 2018. URL: <https://www.sciencedirect.com/science/article/pii/S0168583X18302301>, doi:10.1016/j.nimb.2018.03.037.

[19] Grant J. Lockwood, Laurence E. Ruggles, Glenn H. Miller, and John A. Halbleib. Calorimetric measurement of electron energy deposition in extended media theory vs experiment. Technical report, SAND79-0414 Report, Sandia National Laboratories, Albuquerque, 1980.

[20] Grant J. Lockwood, Laurence E. Ruggles, Glenn H. Miller, and John A. Halbleib. Electron energy and charge albedos calorimetric measurement vs monte carlo theory. Technical report, SAND80-1968 Report, Sandia National Laboratories, Albuquerque, 1981.

[21] M. Moszyński, M. Kapusta, D. Wolski, W. Klamra, and B. Cederwall. Properties of the yap : Ce scintillator. *Nuclear Instruments and Methods in Physics Research Section A: Accelerators, Spectrometers, Detectors and Associated Equipment*, 404(1):157–165, 1998. URL: <https://www.sciencedirect.com/science/article/pii/S0168900297011157>, doi:10.1016/S0168-9002(97)01115-7.

[22] W. Mengesha, T.D. Taulbee, B.D. Rooney, and J.D. Valentine. Light yield nonproportionality of csi(tl), csi(na), and yap. *IEEE Transactions on Nuclear Science*, 45(3):456, 1998. doi:10.1109/23.682426.

[23] GANIL E815S_20 collaboration. Ganil-2021-e815_20 dataset. URL: https://u.ganil-spiral2.eu/10.26143/GANIL-2021-E815_20.

[24] M. Kanafani, X. Fléchard, O. Naviliat-Cuncic, G. D. Chung, S. Leblond, E. Liénard, X. Mougeot, G. Quéméner, A. Simancas Di Filippo, and J.-C. Thomas. High-precision measurement of the ${}^6\text{He}$ half-life. *Phys. Rev. C*, 106:045502, Oct 2022. URL: <https://link.aps.org/doi/10.1103/PhysRevC.106.045502>, doi:10.1103/PhysRevC.106.045502.

[25] FASTER. URL: <https://faster.in2p3.fr/>.

[26] TRIM. URL: <https://www.srim.org/>.

[27] Mohamad Kanafani. *Precision measurements in the beta decay of ${}^6\text{He}$* . PhD thesis, Normandie Université, November 2023. URL: <https://theses.hal.science/tel-04466399>.

[28] L. Urban. A model for multiple scattering in geant4. Technical report, CERN-OPEN-2006-077, CERN, Geneva, Dec 2006. URL: <http://cds.cern.ch/record/1004190>.

[29] Mihaly Novak. On the new and accurate (Goudsmit-Saunderson) model for describing e^-/e^+ multiple Coulomb scattering (Geant4 technical note), 2024. URL: <https://arxiv.org/abs/2410.13361>, arXiv:2410.13361.